High-fidelity 3D live-cell nanoscopy through data-driven enhanced super-resolution radial fluctuation

Romain F. Laine[1-4 *], Hannah S. Heil[5 *], Simao Coelho[5], Jonathon Nixon-Abell[6,7], Angélique Jimenez[8], Tommaso Galgani[9], Aki Stubb[10,11], Gautier Follain[10,12], Siân Culley[1,13], Guillaume Jacquemet[10,12,14], Bassam Hajj[9] ✉, Christophe Leterrier[8] ✉, and Ricardo Henriques[1-3,5,15] ✉

[1]MRC-Laboratory for Molecular Cell Biology, University College London, London, UK
[2]Department of Cell and Developmental Biology, University College London, London, UK
[3]The Francis Crick Institute, London, UK
[4]Current affiliation: MicrographiaBio, Translation Innovation Hub, 84 Wood Lane, London, W12 0BZ
[5]Instituto Gulbenkian de Ciência, Oeiras, Portugal
[6]Janelia Research Campus, Howard Hughes Medical Institute, Ashburn, VA, USA
[7]CIMR, Cambridge Univeristy, Cambridge, UK
[8]NeuroCyto, Aix Marseille Université, CNRS, INP UMR7051, Marseille, France
[9]Laboratoire Physico-Chimie Curie, Institut Curie, PSL Research University, Sorbonne Université, CNRS UMR168, Paris, France
[10]Turku Bioscience Centre, University of Turku and Åbo Akademi University, Turku, Finland
[11]Current affiliation: Helsinki Institute of Life Science, Biomedicum Helsinki, University of Helsinki, 00290 Helsinki, Finland
[12]Faculty of Science and Engineering, Cell Biology, Åbo Akademi University, Turku, Finland
[13]Current affiliation: Randall Centre for Cell Molecular Biophysics, King's College London, Guy's Campus, London SE1 1UL, UK
[14]Turku Bioimaging, University of Turku and Åbo Akademi University, Turku, Finland
[15]Institute for the Physics of Living Systems, University College London, London, UK
[*]Equal contributing authors

In recent years, the development of new image analysis approaches has highlighted the possibility of recovering super-resolution information from short sequences of wide-field images. Our recently developed method, SRRF (Super-Resolution Radial Fluctuations), enables long-term live-cell imaging beyond the resolution limit without specialized hardware. Here, we present eSRRF (enhanced-SRRF), a significant improvement over our initial method, enhancing image fidelity to the underlying structure and resolution. Especially, eSRRF uses automated data-driven parameter optimization, including an estimation of the number of frames necessary for optimal reconstruction. We demonstrate the improved fidelity of the images reconstructed with eSRRF, and highlight its versatility and ease of use over a wide range of microscopy techniques and biological systems. We also extend eSRRF to 3D super-resolution microscopy by combining it with multi-focus microscopy (MFM), obtaining volumetric super-resolution imaging of live cells with acquisition speed of ∼1 volume/second.

Super-resolution Microscopy | Open source | Live-cell 3D imaging

Correspondence:
bassam.hajj@curie.fr, christophe.leterrier@univ-amu.fr and rjhenriques@igc.gulbenkian.pt

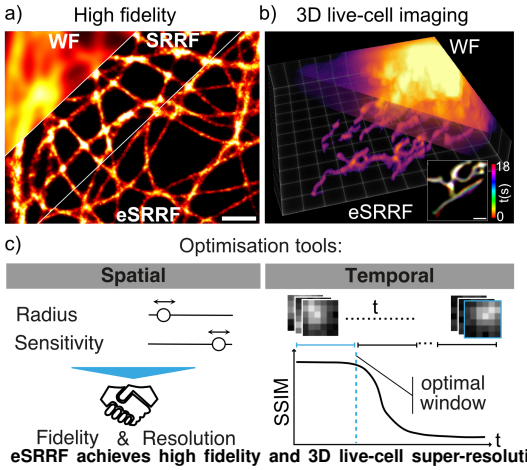

Fig. 1. eSRRF achieves high fidelity and 3D live-cell super-resolution. a) The improved reconstruction algorithm of eSRRF surpasses the performance of the original SRRF processing in both image fidelity and resolution (FRC: SRRF 119±32 nm, eSRRF 84±9 nm). b) eSRRF processing also extends to the axial dimension, thus, achieving volumetric live-cell super-resolution imaging in all three dimensions. c) The integrated optimisation toolbox allows to determine optimal reconstruction parameters to maintain high fidelity and resolution (spatial optimisation tool); and to estimate the temporal window size (temporal optimisation tool). Scale bars in a) and the inset in b) 1 µm.

Introduction

Over the last two decades, super-resolution microscopy (SRM) developments have enabled the unprecedented observation of nanoscale structures in biological systems by light microscopy (1). Stimulated emission depletion (STED) microscopy (2) has led to fast SRM on small fields-of-view with resolution down to 40-50 nm. In contrast, structured illumination microscopy (SIM) (3) provides a doubling in resolution compared to wide-field imaging (∼120 nm) at relatively high-speed and large fields-of-view. Both super-resolution methods rely on complex optical systems to create specific illumination patterns. Single-molecule localization microscopy (SMLM) methods such as (direct) stochastic optical reconstruction microscopy ((d)STORM) (4, 5), photo-activated localization microscopy (PALM) (6) or (DNA-)PAINT (7, 8), take a different approach of stochastic ON/OFF switching. By sequentially localizing single-emitter events, a near molecular resolution (∼10-20 nm) is achieved. However, this commonly requires long acquisition times that range from minutes to hours. Image processing and reconstruction tools including multi-emitter fitting localization algorithms (9), Haar wavelet kernel (HAWK) analysis (10), or deep learning assisted tools (11–13) re-

duce acquisition times by allowing for higher emitter density conditions. Alternatively, fluctuation-based approaches such as super-resolution radial fluctuations (SRRF) (14), super-resolution optical fluctuation imaging (SOFI) (15), multiple signal classification algorithm (MUSICAL) (16) or super-resolution with auto-correlation two-step deconvolution (SACD) (17) can extract super-resolution information from diffraction-limited data (See also Supplementary Table 1). These fluctuation-based approaches only require subtle frame-to-frame intensity variations, rather than the discrete blinking events needed in SMLM, and as such do not require high illumination power densities. Thus, so long as images are acquired with sufficiently high sampling to capture spatial and temporal intensity variations, these methods are compatible with most research-grade fluorescence microscopes. This makes them ideally suited for long-term live-cell SRM imaging.

SRRF is a versatile approach that achieves live-cell SRM on a wide range of available microscopy platforms with commonly used fluorescent protein tags (18). It is now a widely used high-density reconstruction algorithm, as highlighted by an important uptake by the community (19–22). The great reception of the SRRF processing tool can also be attributed to its user-friendly implementation, and high accessibility within the Fiji framework (23). However, obtaining optimal reconstruction results with fluctuation-based analysis tools is challenging as they can suffer from reconstruction artifacts and lack signal linearity . Previously, we have developed an approach for the detection and quantification of image artifacts termed SQUIRREL (24). This tool has rapidly become a gold standard in the quantification of super-resolution image quality (25), providing an important platform to assist in the creation of new algorithms, such as those implementing Deep Learning-based methods (26, 27).

Here, we present a novel implementation of the SRRF approach termed enhanced SRRF (eSRRF) and highlight its improved capabilities in terms of image fidelity, resolution, and user-friendliness (Figure 1). In eSRRF, we redefined some of the fundamental principles used to estimate radiality and temporal analysis to achieve an improved image quality of the reconstructions. Our new implementation integrates the SQUIRREL engine to provide an automated exploration of the parameter space which identifies the optimal reconstruction parameter set based on quantitative measures of image fidelity and resolution. By highlighting the optimal parameter and acquisition configurations, eSRRF minimizes artifacts and non-linearity. Therefore, eSRRF improves overall image fidelity with respect to the underlying structure. The enhanced performance is verified over a wide range of emitter densities and imaging modalities, whilst reducing user bias.

We have additionally implemented a new capacity to achieve full 3D resolution improvement, bypassing the constraints of 2D only of the original SRRF. The axial dimension still is a weak point in live cell super-resolution microscopy: current implementations of 3D super-resolution methods come at the expense of a limited axial range and long acquisition times, often including major technical demands (28–31).

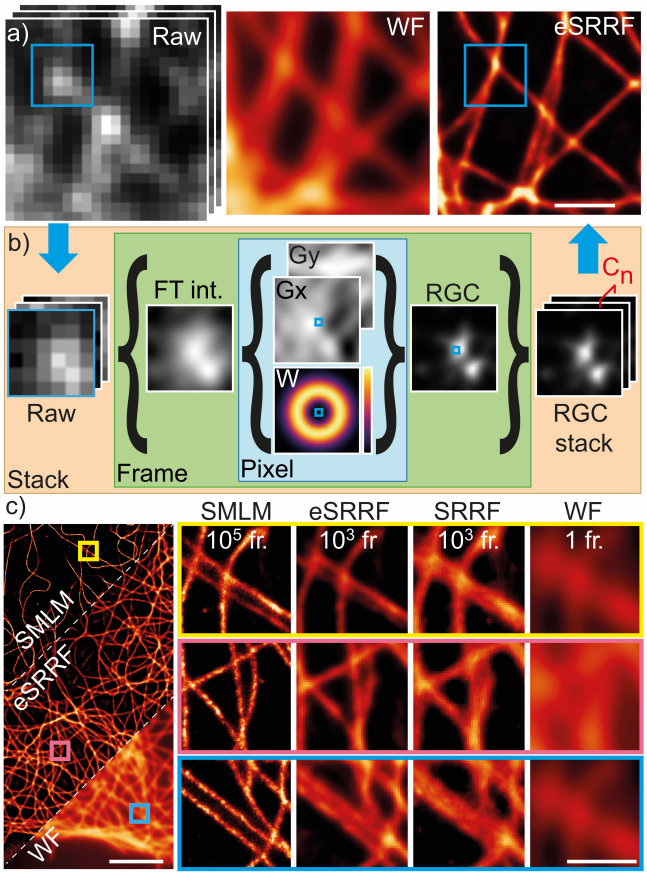

Fig. 2. eSRRF image reconstruction produces high-fidelity images. a) eSRRF processing based on a raw data image stack (Raw, left) of a microtubule network allows to surpass the diffraction limited wide-field (WF, middle) image resolution and to super-resolve features that were hidden before (eSRRF, right). b) eSRRF reconstruction steps: Each frame in the stack is interpolated (Fourier transform interpolation, FT int.), from which the gradients *Gx* and *Gy* are calculated. The corresponding weighting factor map *W* is created based on the set radius *R*. Based on this, the radial gradient convergence (RGC) is calculated for each pixel to compute the RGC map. The RGC stack is then compressed into a super-resolution image by cross-correlation (C_n). c) Super-resolved reconstruction images from eSRRF and SRRF obtained from 1000 frames of high density fluctuation data, created in-silico from an experimental sparse emitter dataset (DNA-PAINT microscopy of immunolabeled microtubules in fixed COS7 cells). The SMLM reconstruction obtained from the sparse data and the wide-field equivalent are shown for comparison.The number of frames used for reconstruction is indicated in each column (FRC resolution estimate: SMLM 71 ± 2 nm, eSRRF 84±11 nm, SRRF 112±40 nm, WF 215 ± 20 nm).

Live-cell super-resolution multidimensional imaging also requires a significantly higher illumination dose than 2D super-resolution images, severely compromising cell health and viability. (32). One approach that allows researchers to speed up the acquisition and thus reduce the total light exposure is multi-focus microscopy (MFM) (33–35). By acquiring multiple focal planes simultaneously, single shot volumetric imaging is realized. As the focal planes are temporally coherent - meaning there is no time lag between axial planes - MFM is particularly well suited for fluctuation-based volumetric live-cell super-resolution imaging, by performing eSRRF on 3D voxels.

Results

eSRRF provides high-fidelity SRM images. The eSRRF algorithm allows for the reconstruction of super-resolution

images with a particular emphasis on image quality. The increased image fidelity results from the implementation of several new and/or optimized routines in the radial fluctuation analysis algorithm, introduced through a full rewriting of the code. In eSRRF, a raw image time-series with fluctuating fluorescence signals is analyzed (Figure 2a). First, each single frame is upsampled by interpolation (Figure 2b). Here, in contrast to standard SRRF, we introduced a new interpolation strategy. eSRRF now exploits a full data interpolation step based on Fourier transform prior to the gradient calculation. This approach outperforms the cubic spline interpolation employed in the original SRRF analysis by minimizing macro-pixel artifacts (Supplementary Figure S1). Second, following the Fourier transform interpolation, intensity gradients Gx and Gy are calculated and the corresponding weighting factor W based on the user defined radius R is generated for each pixel. Based on gradient and weighting maps and the user defined sensitivity (S) parameter (Supplementary Note 1), the radial gradient convergence (RGC) is estimated. Thus, in the case of eSRRF, this estimation is not just based on a set number of points at a specific radial distance as it was handled by the previous implementation of SRRF, but over a wider area. This area and how each point contributes to the RGC metric is defined by the W-map. This allows to cover the size of the Point Spread Function (PSF) of the imaging system and, thus, to exploit the local environment of the pixel of interest much more efficiently. Auto- and/or cross-correlation of the resulting RGC time series allows to reconstruct a super-resolved image which shows high fidelity with respect to the underlying structure (Figure 2b). Compared to the original SRRF, our new eSRRF approach demonstrates a clear improvement in image quality (Figure 2c, Supplementary Figure S2 & S3 and Supplementary Note 2). Although these new implementations make eSRRF processing computationally more demanding, the implementation of openCL to parallelise calculations and minimize processing time allows the use of all available computing resources at their peak performance regardless of the platform used.

To evaluate the fidelity of eSRRF with respect to the underlying structure, we performed analysis of a DNA-PAINT dataset with sparse localizations. For DNA-PAINT, standard SMLM localization algorithms applied to the raw, sparse data can provide an accurate representation of the underlying structure. By temporally binning the raw data, we generated a high-density dataset comparable to a typical live-cell imaging acquisition. Figure 2c shows the comparison of the ground-truth (SMLM), eSRRF, SRRF and equivalent wide-field (WF) data. eSRRF is in good structural agreement with the ground truth and shows a clear resolution improvement over both the wide-field and the SRRF reconstruction. Line profiles reveal that eSRRF resolves features that were only visible in the SMLM reconstruction (Supplementary Figure S2). This observation is supported by the estimation of the image resolution by Fourier Ring Correlation (FRC) (36), which provides a quantitative assessment of the performance of the different image reconstruction modalities. Furthermore, the enhanced image fidelity recovered from eSRRF is

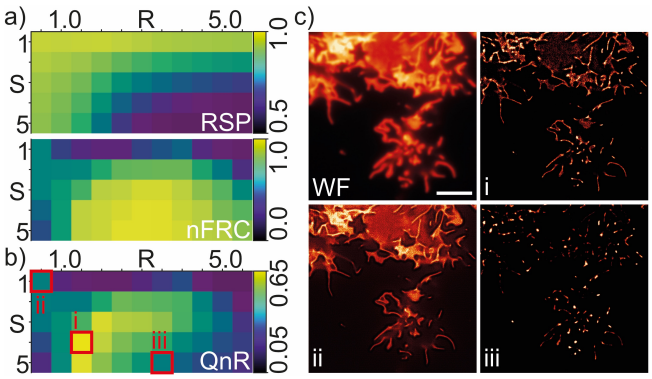

Fig. 3. eSRRF provides an automated reconstruction parameter search. a) RSP and FRC resolution maps as functions of Radius (R) and Sensitivity (S) reconstruction parameters. b) Combined QnR metric map showing the compromise between fidelity and FRC resolution. c) Wide-field image, optimal reconstruction (i, R=1.5, S=4), low resolution reconstruction (ii, R=0.5, S=1) and low fidelity reconstruction (iii, R=3.5, S=5). TIRF images dataset of COS-7 cells, labeled with membrane targeting domain of Lyn kinase – SkylanS from Moeyaert et al. (38). Scale bar: 20 µm.

quantitatively confirmed using SQUIRREL analysis on both simulated and experimental data (Supplementary Figures S3 & S4, Supplementary Note 2).

eSRRF not only achieves higher fidelity in image reconstruction than the previous SRRF application, but also provides a robust and reproducible reconstruction method over a wide range of emitter densities. To estimate the range of emitter densities compatible with eSRRF, we again use low-density DNA-PAINT acquisitions and temporally binned the images with varying numbers of frames per bin. By increasing the number of frames per bin, the density of molecules in each binned frame is higher. Whilst the total number of molecules remains consistent throughout, this approach allows us to monitor the performance of eSRRF as a function of emitter density. Supplementary Figure S5 presents the results from this analysis across the 3 temporal analyses provided (AVG, TAC2, VAR, see Supplementary Note 3). For each density range, a specific set of the processing parameters will provide the best image quality (see Supplementary Notes 1 3) allowing access to high fidelity super-resolved image reconstructions across a wide range of experimental conditions and emitter fluctuation densities. At high emitter densities, eSRRF also outperforms the high-density emitter localization algorithm of ThunderSTORM (37) even in combination with HAWK analysis (10) (Supplementary Figure S6). At low densities, single emitter fitting still provides unsurpassed localization precision and image resolution; however, it requires the processing of a large number of images. Here, eSRRF can provide a fast preview of the reconstructed image (Supplementary Figure S7).

eSRRF provides an adaptable reconstruction parameter exploration scheme. The decision to use a specific set of parameters for an image reconstruction is often based on user bias. This can lead to the inclusion of artifacts in the data (10). Here, we develop a quantitative reconstruction parameter search based on SQUIRREL. The user is provided with a visual map of the eSRRF parameter space of radius R and sensitivity S with respect to achievable resolution and image

fidelity. In our SQUIRREL algorithm, we use FRC to determine image resolution and Resolution-scaled Pearson correlation coefficient (RSP) as a metric for image fidelity. The approach consists of scanning the two main parameters of eSRRF (the radius R and the sensitivity S, defining the RS parameter space) across a reasonable range in search for an optimal trade-off between FRC resolution and RSP fidelity. An optimal condition can be found by combining the two metrics into a single balanced metric, termed QnR score:

$$QnR = \frac{2 \times RSP \times nFR}{RSP + nFRC}$$

Here nFRC is the normalized FRC resolution metric, ranging between 0 and 1, with 0 representing a poor resolution and 1 representing a high resolution.

The QnR score ranges between 0 and 1, where scores close to 1 represent a good combination of FRC resolution and RSP fidelity, whereas a QnR score close to 0 represents a low-quality image reconstruction. Figure 3 shows a representative dataset acquired with COS7 cells expressing lyn kinase – SkylanS previously published by Moeyaerd et al. (38, 39). The eSRRF parameter scan analysis (Figure 3a) shows how the RSP fidelity and the FRC resolution are combined within the RS parameters space. RSP fidelity is high when using a low sensitivity and/or low radius. In contrast, FRC resolution improves upon increasing the sensitivity over a large range of radii. This can be explained by the appearance of nonlinear artifacts at high sensitivity leading to low RSP fidelity but high FRC resolution. In addition, as the radius increases, the resolution of the reconstructed image decreases. The QnR metric map, shown in Figure 3b, demonstrates that a balance can be found that leads to good resolution and fidelity. Figure 3c shows a range of image reconstruction parameters: the optimal reconstruction parameter set (R=1.5, S=4, Figure 3c, i) and two other suboptimal parameter sets (Figure 3c ii and iii). Figure 3c ii shows a low-resolution image, whereas Figure 3c iii has a high level of non-linearity - the result of an inappropriately high sensitivity. Our automated parameter search implemented in eSRRF enables the user to find the optimal settings for the specific dataset being analyzed. Therefore, our data-driven optimization provides the best parameters for both fidelity and spatial resolution.

An important aspect of live-cell super-resolution imaging is its capacity for observation and quantification of dynamic processes at the molecular level. To address this, we have further integrated temporal structural similarity (tSSIM) analysis (Supplementary Figure S8). Here, we calculate the progression of the structural similarity (40) at the different time points of the image stack relative to the first frame. This allows us to identify the local molecular dynamics and estimate the maximum number of frames within which the structural similarity is retained -meaning there is no observable movement. By combining tSSIM with eSRRF, we can determine the optimal temporal sampling rate required to recover such dynamics, whilst avoiding motion blur artifacts (Supplementary Figure S9).

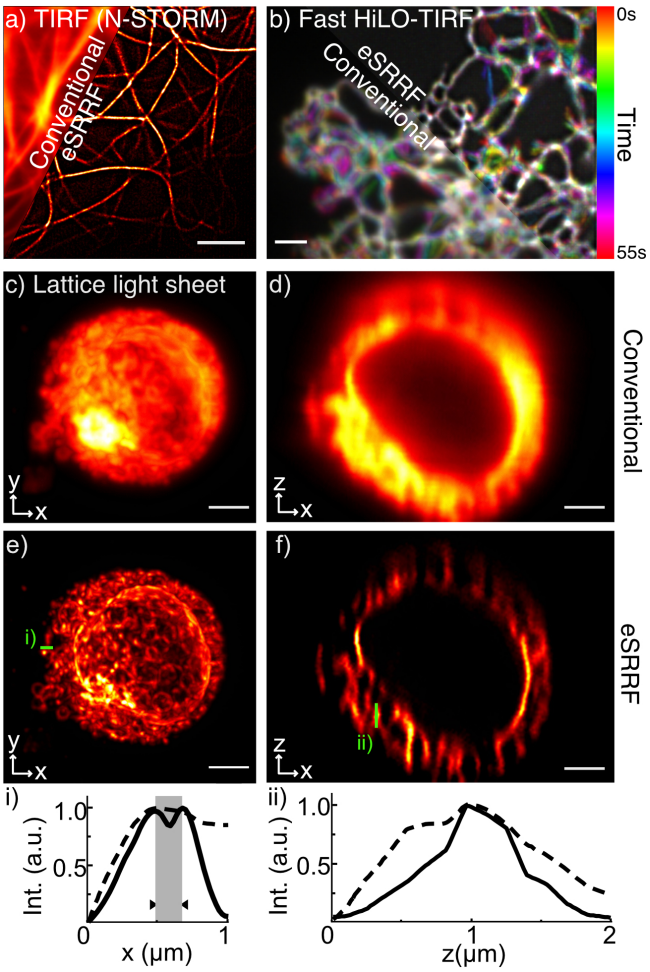

Fig. 4. Applications of eSRRF to a range of imaging modalities. a) Live-cell TIRF imaging of HeLa cells expressing ffDronpa-MAP4 (FRC resolution Conventional/eSRRF: 266±51/128±51 nm). b) Live-cell HiLO-TIRF of COS-7 cells expressing PrSS-mEmerald-KDEL marking the ER lumen. The temporal evolution is color-coded (FRC resolution Conventional/eSRRF: 254±11/143±56 nm). c-f) Lattice light sheet (LLS) imaging of the ER in live Jurkat cells at a rate of 7.6 mHz per volume (79 x 55 x 35 µm3). c, xy projection, and d, xz projection using LLS microscopy. e, xy projection, and f, xz projection using eSRRF reconstruction. As the acquisition, the eSRRF processing was applied on a slice-by-slice basis. Line profiles corresponding to the x- and z-direction are shown in i and ii, respectively. The line profile in i reveals sub-diffraction features separated by 190 nm (marked in gray) (FRC resolution LLS/eSRRF: 164±9/84±43 nm). Scale bar in a) 5 µm, b) 2 µm and c-f) 3 µm.

eSRRF works across a wide range of live-cell imaging modalities. Here, we test our approach on a wide range of imaging modalities including total internal reflection fluorescence (TIRF), fast highly inclined and laminated optical sheet (HiLO)-TIRF (41), spinning-disk confocal (SDC) (42) and lattice light-sheet (LLS) microscopy (43). We show that eSRRF provides high quality live-cell SRM images (Figure 4). First, we imaged ffDronpa-MAP4 in live HeLa cells using TIRF microscopy. eSRRF reconstruction, performed post-acquisition, allows for a super-resolved view of the microtubule network in living cells (Figure 4a). Second, we evaluated the dynamic rearrangement of the endoplasmic reticulum (ER) in living COS-7 cells. Acquired using HiLO-TIRF, the fast acquisition rates allowed us to track the ER network tagged with PrSS-mEmerald-KDEL, at super-resolution level (Figure 4b). Here, a sampling rate of 50 ms is achieved using rolling window analysis of eSRRF (Supplementary Fig-

ure S10). While TIRF and HiLO-TIRF imaging are set out for fast high contrast imaging in close vicinity to the coverslip surface, SDC excels in fast and gentle in vivo imaging. This entails imaging far away from the coverslip and deep inside challenging samples as spheroids and live organisms where eSRRF achieves enhanced performance as well (Supplementary Figure S11).

eSRRF can also be applied to volumetric live-cell datasets as obtained for example with LLS microscopy (Supplementary Movie 1). Here, the eSRRF reconstruction of volumetric image stacks is obtained by processing each slice sequentially. Note that this approach can only effectively improve the lateral resolution (x-y plane), while there is a sharpening comparable to deconvolution in the z-direction, there are no sub-diffraction limited features evident. This can be for example observed in Figure 4 c-f) where the plane by plane eSRRF processing of a LLS dataset of the ER in live Jurkat cells allows to distinguish sub-diffraction limited features along the x-direction (Figure 4e), line profile i)), but not in the z-direction (Figure 4f), line profile ii)).

Volumetric live-cell super-resolution imaging by eSRRF in combination with multifocus microscopy. 3D imaging capability is becoming increasingly more important to understand molecular dynamics and interactions within the full context of their environment. In particular, obtaining true 3D SRM with improved resolution along the axial direction has recently become a key focus of development. Fluctuation-based SRM approaches have also been extended to 3D, notably SOFI (15, 44) and, more recently, random illumination microscopy (RIM) (45), an approach that combines the concepts of fluctuation microscopy and the SIM demodulation principle. To realize 3D eSRRF, we extended the algorithm to calculate the RGC in 3D. Consequently, we can reconstruct a volumetric image with enhanced resolution in the axial direction at the same time as in the lateral image plane. The approach was first validated with a simulated 3D dataset (see Supplementary Figure S12). In practice, extending fluctuation-based analysis methods to 3D requires the near-simultaneous detection of multiple planes. To determine the radial symmetry in 3D, within the time scale of the temporal fluctuations of the fluorescent probes, the whole volume needs to be acquired concurrently. MFM allows for the detection of multiple axial planes onto a single camera at the same time by using an aberration corrected diffractive optical element (33–35) (Supplementary Figure S13). By combining MFM and eSRRF, a super-resolved volumetric view (20 x 20 x 3.6 µm3) of the mitochondrial network architecture and dynamics in U2OS cells was acquired at a rate of 1Hz (Figure 5). The eSRRF processing achieved super-resolution in lateral and axial dimensions, revealing sub-diffraction limited structures. Figure 5 shows that eSRRF reveals structures which would otherwise remain undetected using conventional MFM, even after applying deconvolution (Figure 5 i-ii) Supplementary Figure S14). By processing the entire image sequence the dynamic fluctuations of the mitochondrial network in the living cell can be observed at super-resolution level over time (Figure 5 iii), Supplementary Movie 23).

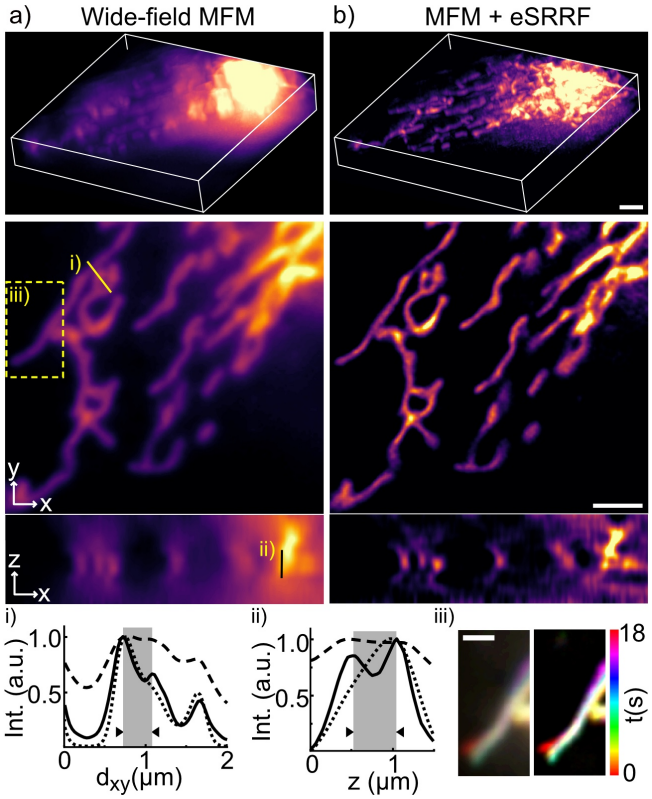

Fig. 5. SRRF and MFM allows 3D live-cell super-resolution. a) Live-cell volumetric imaging in MFM widefield configuration of U2OS cells expressing TOM20-Halo, loaded with JF549. b) 3D eSRRF processing of the dataset creates a super-resolved volumetric view of 20 x 20 x 3.6 µm3 at a rate of 1Hz (MFM + eSRRF). a-b) Top: 3D rendering, middle: single cropped z-slice (FRC resolution in xy: interpolated: 231 ± 10 nm, eSRRF: 74 ± 12 nm), bottom: single cropped y-slice (xz eSRRF: 173 ± 19 nm) with i) and ii) mark the positions of the respective line profiles in x,y and z-plane in the MFM (dashed line), deconvolved MFM (dotted line, see Supplementary Figure S14) and MFM+eSRRF (solid line) images. The distance of the structures resolved by eSRRF processing (marked gray) is 360 nm in the lateral directions (x,y) and 500 nm in the axial direction (z). iii) marks the displayed area of the temporal color coded projection of a single z slice over the whole MFM (left) and MFM+eSRRF (right) acquisition. Scale bars 2 µm in a-b) and 1 µm in iii).

Conclusion

The new optimized and extended eSRRF image processing approach provides a significant improvement in image reconstruction quality and fidelity from fluorescence fluctuation microscopy data compared to the original SRRF implementation, as well as in useability of the method, thanks to its data-driven parameter optimisation companion tools. We demonstrated the approach on microscopy datasets obtained from a wide range of imaging platforms and techniques from widefield, TIRF, light sheet, spinning-disc confocal and SMLM imaging modalities. Furthermore, eSRRF shows robust performance over the different signal fluctuation dynamics displayed by various organic dyes and fluorescent proteins and over a wide range of marker densities. To achieve optimal spatial and temporal resolution, minimize reconstruction artifacts and reduce user bias, we have implemented a metric for image resolution and fidelity, which we call QnR, which is used to perform data-driven parameter optimization alongside temporal window optimisation. This makes eSRRF the first super-resolution image reconstruction approach provid-

ing the user with optimal processing parameters - ideal for live-cell super-resolution- and to minimize total light exposure by fast acquisition speeds and low excitation power densities. By implementing the eSRRF tool as a Fiji plugin, with GPU acceleration along with a detailed user guide, we provide an easy-to-use open-source and free-to-access package for the bioimaging community. The additional implementation of the radial fluctuation analysis in 3D provides a unique combination of live-cell, volumetric imaging, with sub-diffraction limited accuracy. The resolution achieved here is surpassed by more complex live-cell 3D SRM microscopy techniques such as 3D RIM (45). Furthermore, implementing 3D eSRRF requires a custom built optical system to ensure the simultaneous detection of several focal planes. On the other hand, as a scanning-free 3D technique, as it has the advantage of providing high speed imaging of larger volumes than can be achieved with 3D RIM, as technically it is only limited by the camera read out. Thus, making the unique combination of 3D eSRRF and MFM set out for fast live-cell 3D super-resolution microscopy.

Availability. eSRRF is available as Supplemental Software or can be accessed from our GitHub page. This resource is fully open-source and includes a Wiki manual and many real-life example datasets for training and testing.

Data availability. Example datasets are available on our GitHub page. Further data are available on request.

ACKNOWLEDGEMENTS

We thank Jennifer Lippincott-Schwartz and Christoher Obara, Janelia Farm, for their assistance with the dynamic ER-TIRF data and for reading the manuscript, Peter Dedecker, University of Leuven, for providing the ffDronpa-MAP4 plasmid and Jesse Goyette and Samantha Webster, University of New South Wales, for their assistance with the lattice light sheet. This work was supported by the Gulbenkian Foundation (H.S.H., S.C. (Coelho), R.H.) and received funding from the European Research Council (ERC) under the European Union's Horizon 2020 research and innovation programme (grant agreement no.101001332 to R.H.), the European Molecular Biology Organization (EMBO-2020-IG-4734 to R.H. and ALTF 499-2021 to H.S.H), the Wellcome Trust (203276/Z/16/Zto R.H.), and NHMRC (APP1183588 to S.C. (Coelho). R.F.L. would like to acknowledge the support of the MRC Skills development fellowship (MR/T027924/1). SC (Culley) would like to acknowledge support from a Royal Society University Research Fellowship. This study was supported by the Academy of Finland (G.J., 338537 and G.F., 332402), the Sigrid Juselius Foundation (G.J.), the Cancer Society of Finland (G.J.), the Åbo Akademi University Research Foundation (G.J., CoE CellMech), the Drug Discovery and Diagnostics strategic funding to Åbo Akademi University (G.J.). The Cell Imaging and Cytometry Core facility (Turku Bioscience, University of Turku, Åbo Akademi University, and Biocenter Finland) and Turku Bioimaging are acknowledged for services, instrumentation, and expertise. C.L. would like to acknowledge funding of CNRS through the ATIP (A0 2016) grant. B.H. acknowledges funding from the Fondation pour la recherche médicale (FRM; DEI20151234398), the Agence National de la recherche (ANR-19-CE42-0003-01), the LabEx CelTisPhyBio (ANR-11-LABX-0038, ANR-10-IDEX-0001-02), the Institut Curie, Agence pour la Recherche sur le Cancer (ARC Foundation), DIM ELICIT and from ITMO Cancer of Aviesan on funds administered by Inserm (grant N° 20CP092-00). B.H. recognizes the support of France-BioImaging infrastructure grant ANR-10-INBS-04 (Investments for the future).

EXTENDED AUTHOR INFORMATION

- Romain F. Laine: 0000-0002-2151-4487; LaineBioImaging
- Hannah S. Heil: 0000-0003-4279-7022; Hannah_SuperRes
- Simao Coelho: 0000-0002-0763-3172; simaopc
- Jonathon Nixon-Abell: 0000-0003-4169-0012; AbellJonny
- Angélique Jimenez
- Tommaso Galgani: 0000-0002-7154-7586;
- Aki Stubb: 0000-0002-4146-9994 akistub
- Gautier Follain: 0000-0003-0495-9529 @Follain_Ga
- Siân Culley: 0000-0003-2112-0143; SuperResoluSian
- Guillaume Jacquemet: 0000-0002-9286-920X; guijacquemet
- Bassam Hajj: 0000-0002-5097-6832; Bassam_A_HAJJ
- Christophe Leterrier: 0000-0002-2957-2032; christlet
- Ricardo Henriques: 0000-0002-2043-5234; HenriquesLab

AUTHOR CONTRIBUTIONS

R.F.L., B.H., C.L and R.H. designed the study. R.F.L., S.C. (Culley), and R.H. wrote the algorithm. S.C. (Culley) wrote the script for data simulation. R.F.L., S.C. (Coelho), H.S.H., J.N-A., A.J., T.G., A.S., G.F., G.J., B.H. and C.L. performed the experiments. H.S.H., tested, documented, and validated the algorithm, and analyzed the data. S.C. (Coelho) analyzed the LLS data. All authors planned experiments and contributed to the writing of the article.

COMPETING FINANCIAL INTERESTS

The authors declare no competing financial interests.

Bibliography

1. Guillaume Jacquemet, Alexandre F. Carisey, Hellyeh Hamidi, Ricardo Henriques, and Christophe Leterrier. The cell biologist's guide to super-resolution microscopy. 133(11). ISSN 0021-9533. doi: 10.1242/jcs.240713.
2. Stefan W. Hell and Jan Wichmann. Breaking the diffraction resolution limit by stimulated emission: stimulated-emission-depletion fluorescence microscopy. 19(11):780. ISSN 0146-9592, 1539-4794. doi: 10.1364/OL.19.000780.
3. Mats G. L. Gustafsson. Surpassing the lateral resolution limit by a factor of two using structured illumination microscopy. SHORT COMMUNICATION. 198(2):82–87. ISSN 0022-2720, 1365-2818. doi: 10.1046/j.1365-2818.2000.00710.x.
4. Mike Heilemann, Sebastian vandeLinde, Mark Schüttpelz, Robert Kasper, Britta Seefeldt, Anindita Mukherjee, Philip Tinnefeld, and Markus Sauer. Subdiffraction-resolution fluorescence imaging with conventional fluorescent probes. 47(33):6172–6176. ISSN 14337851, 15213773. doi: 10.1002/anie.200802376.
5. Michael J Rust, Mark Bates, and Xiaowei Zhuang. Sub-diffraction-limit imaging by stochastic optical reconstruction microscopy (STORM). 3(10):793–796. ISSN 1548-7091, 1548-7105. doi: 10.1038/nmeth929.
6. Eric Betzig, George H. Patterson, Rachid Sougrat, O. Wolf Lindwasser, Scott Olenych, Juan S. Bonifacino, Michael W. Davidson, Jennifer Lippincott-Schwartz, and Harald F. Hess. Imaging intracellular fluorescent proteins at nanometer resolution. 313(5793):1642–1645. ISSN 0036-8075, 1095-9203. doi: 10.1126/science.1127344.
7. Ralf Jungmann, Christian Steinhauer, Max Scheible, Anton Kuzyk, Philip Tinnefeld, and Friedrich C. Simmel. Single-molecule kinetics and super-resolution microscopy by fluorescence imaging of transient binding on DNA origami. 10(11):4756–4761. ISSN 1530-6984, 1530-6992. doi: 10.1021/nl103427w.
8. Alexey Sharonov and Robin M. Hochstrasser. Wide-field subdiffraction imaging by accumulated binding of diffusing probes. 103(50):18911–18916. ISSN 0027-8424, 1091-6490. doi: 10.1073/pnas.0609643104.
9. Daniel Sage, Thanh-An Pham, Hazen Babcock, Tomas Lukes, Thomas Pengo, Jerry Chao, Ramraj Velmurugan, Alex Herbert, Anurag Agrawal, Silvia Colabrese, Ann Wheeler, Anna Archetti, Bernd Rieger, Raimund Ober, Guy M. Hagen, Jean-Baptiste Sibarita, Jonas Ries, Ricardo Henriques, Michael Unser, and Seamus Holden. Super-resolution fight club: assessment of 2d and 3d single-molecule localization microscopy software. 16(5):387–395. ISSN 1548-7091, 1548-7105. doi: 10.1038/s41592-019-0364-4.
10. Richard J. Marsh, Karin Pfisterer, Pauline Bennett, Liisa M. Hirvonen, Mathias Gautel, Gareth E. Jones, and Susan Cox. Artifact-free high-density localization microscopy analysis. 15(9):689–692. ISSN 1548-7091, 1548-7105. doi: 10.1038/s41592-018-0072-5.
11. Elias Nehme, Daniel Freedman, Racheli Gordon, Boris Ferdman, Lucien E. Weiss, Onit Alalouf, Tal Naor, Reut Orange, Tomer Michaeli, and Yoav Shechtman. DeepSTORM3d: dense 3d localization microscopy and PSF design by deep learning. 17(7):734–740. ISSN 1548-7091, 1548-7105. doi: 10.1038/s41592-020-0853-5.
12. Wei Ouyang, Andrey Aristov, Mickaël Lelek, Xian Hao, and Christophe Zimmer. Deep learning massively accelerates super-resolution localization microscopy. 36(5):460–468. ISSN 1087-0156, 1546-1696. doi: 10.1038/nbt.4106.
13. Artur Speiser, Lucas-Raphael Müller, Philipp Hoess, Ulf Matti, Christopher J. Obara, Wesley R. Legant, Anna Kreshuk, Jakob H. Macke, Jonas Ries, and Srinivas C. Turaga. Deep learning enables fast and dense single-molecule localization with high accuracy. 18(9): 1082–1090. ISSN 1548-7091, 1548-7105. doi: 10.1038/s41592-021-01236-x.
14. Nils Gustafsson, Siân Culley, George Ashdown, Dylan M. Owen, Pedro Matos Pereira, and Ricardo Henriques. Fast live-cell conventional fluorophore nanoscopy with ImageJ through super-resolution radial fluctuations. 7(1):12471. ISSN 2041-1723. doi: 10.1038/ncomms12471.
15. T. Dertinger, R. Colyer, G. Iyer, S. Weiss, and J. Enderlein. Fast, background-free, 3d super-resolution optical fluctuation imaging (SOFI). 106(52):22287–22292. ISSN 0027-8424, 1091-6490. doi: 10.1073/pnas.0907866106.
16. Krishna Agarwal and Radek Macháň. Multiple signal classification algorithm for super-resolution fluorescence microscopy. 7(1):13752. ISSN 2041-1723. doi: 10.1038/ncomms13752.
17. Weisong Zhao, Jian Liu, and Haoyu Li. Ultrafast super-resolution imaging via autocorrelation two-step deconvolution. In *Ultrafast Nonlinear Imaging and Spectroscopy VIII*, volume 11497, pages 42–49. SPIE. doi: 10.1117/12.2567853.
18. Siân Culley, Kalina L. Tosheva, Pedro Matos Pereira, and Ricardo Henriques. SRRF: Universal live-cell super-resolution microscopy. 101:74–79, . ISSN 13572725. doi: 10.1016/j.biocel.2018.05.014.
19. Gautam Dey, Siân Culley, Scott Curran, Uwe Schmidt, Ricardo Henriques, Wanda Kukulski, and Buzz Baum. Closed mitosis requires local disassembly of the nuclear envelope. 585 (7823):119–123. ISSN 0028-0836, 1476-4687. doi: 10.1038/s41586-020-2648-3.
20. Mary Ecke, Jana Prassler, Patrick Tanribil, Annette Müller-Taubenberger, Sarah Körber, Jan Faix, and Günther Gerisch. Formins specify membrane patterns generated by propagating actin waves. 31(5):373–385. ISSN 1059-1524, 1939-4586. doi: 10.1091/mbc.E19-08-0460.

21. Stephen D. Grant, Gemma S. Cairns, Jordan Wistuba, and Brian R. Patton. Adapting the 3d-printed openflexure microscope enables computational super-resolution imaging. 8:2003. ISSN 2046-1402. doi: 10.12688/f1000research.21294.1.
22. Aki Stubb, Romain F. Laine, Mitro Miihkinen, Hellyeh Hamidi, Camilo Guzmán, Ricardo Henriques, Guillaume Jacquemet, and Johanna Ivaska. Fluctuation-based super-resolution traction force microscopy. 20(4):2230–2245. ISSN 1530-6984, 1530-6992. doi: 10.1021/acs.nanolett.9b04083.
23. Johannes Schindelin, Ignacio Arganda-Carreras, Erwin Frise, Verena Kaynig, Mark Longair, Tobias Pietzsch, Stephan Preibisch, Curtis Rueden, Stephan Saalfeld, Benjamin Schmid, Jean-Yves Tinevez, Daniel James White, Volker Hartenstein, Kevin Eliceiri, Pavel Tomancak, and Albert Cardona. Fiji: an open-source platform for biological-image analysis. 9(7): 676–682. ISSN 1548-7091, 1548-7105. doi: 10.1038/nmeth.2019.
24. Siân Culley, David Albrecht, Caron Jacobs, Pedro Matos Pereira, Christophe Leterrier, Jason Mercer, and Ricardo Henriques. Quantitative mapping and minimization of super-resolution optical imaging artifacts. 15(4):263–266, . ISSN 1548-7091, 1548-7105. doi: 10.1038/nmeth.4605.
25. Sebastian van de Linde. Single-molecule localization microscopy analysis with ImageJ. 52 (20):203002. ISSN 0022-3727, 1361-6463. doi: 10.1088/1361-6463/ab092f.
26. Linjing Fang, Fred Monroe, Sammy Weiser Novak, Lyndsey Kirk, Cara R. Schiavon, Seungyoon B. Yu, Tong Zhang, Melissa Wu, Kyle Kastner, Alaa Abdel Latif, Zijun Lin, Andrew Shaw, Yoshiyuki Kubota, John Mendenhall, Zhao Zhang, Gulcin Pekkurnaz, Kristen Harris, Jeremy Howard, and Uri Manor. Deep learning-based point-scanning super-resolution imaging. 18(4):406–416. ISSN 1548-7091, 1548-7105. doi: 10.1038/s41592-021-01080-z.
27. Luhong Jin, Bei Liu, Fenqiang Zhao, Stephen Hahn, Bowei Dong, Ruiyan Song, Timothy C. Elston, Yingke Xu, and Klaus M. Hahn. Deep learning enables structured illumination microscopy with low light levels and enhanced speed. 11(1):1934. ISSN 2041-1723. doi: 10.1038/s41467-020-15784-x.
28. Bo Huang, Wenqin Wang, Mark Bates, and Xiaowei Zhuang. Three-dimensional super-resolution imaging by stochastic optical reconstruction microscopy. 319(5864):810–813. ISSN 0036-8075, 1095-9203. doi: 10.1126/science.1153529.
29. Lin Shao, Peter Kner, E Hesper Rego, and Mats G L Gustafsson. Super-resolution 3d microscopy of live whole cells using structured illumination. 8(12):1044–1046. ISSN 1548-7091, 1548-7105. doi: 10.1038/nmeth.1734.
30. Gleb Shtengel, James A. Galbraith, Catherine G. Galbraith, Jennifer Lippincott-Schwartz, Jennifer M. Gillette, Suliana Manley, Rachid Sougrat, Clare M. Waterman, Pakorn Kanchanawong, Michael W. Davidson, Richard D. Fetter, and Harald F. Hess. Interferometric fluorescent super-resolution microscopy resolves 3d cellular ultrastructure. 106(9):3125–3130. ISSN 0027-8424, 1091-6490. doi: 10.1073/pnas.0813131106.
31. Lexy von Diezmann, Yoav Shechtman, and W. E. Moerner. Three-dimensional localization of single molecules for super-resolution imaging and single-particle tracking. 117(11):7244–7275. ISSN 0009-2665, 1520-6890. doi: 10.1021/acs.chemrev.6b00629.
32. William C. Lemon and Katie McDole. Live-cell imaging in the era of too many microscopes. 66:34–42. ISSN 09550674. doi: 10.1016/j.ceb.2020.04.008.
33. Sara Abrahamsson, Jiji Chen, Bassam Hajj, Sjoerd Stallinga, Alexander Y Katsov, Jan Wisniewski, Gaku Mizuguchi, Pierre Soule, Florian Mueller, Claire Dugast Darzacq, Xavier Darzacq, Carl Wu, Cornelia I Bargmann, David A Agard, Maxime Dahan, and Mats G L Gustafsson. Fast multicolor 3d imaging using aberration-corrected multifocus microscopy. 10(1):60–63. ISSN 1548-7091, 1548-7105. doi: 10.1038/nmeth.2277.
34. Bassam Hajj, Jan Wisniewski, Mohamed El Beheiry, Jiji Chen, Andrey Revyakin, Carl Wu, and Maxime Dahan. Whole-cell, multicolor superresolution imaging using volumetric multifocus microscopy. 111(49):17480–17485, . ISSN 0027-8424, 1091-6490. doi: 10.1073/pnas.1412396111.
35. Bassam Hajj, Laura Oudjedi, Jean-Bernard Fiche, Maxime Dahan, and Marcelo Nollmann. Highly efficient multicolor multifocus microscopy by optimal design of diffraction binary gratings. 7(1):5284, . ISSN 2045-2322. doi: 10.1038/s41598-017-05531-6.
36. Robert P J Nieuwenhuizen, Keith A Lidke, Mark Bates, Daniela Leyton Puig, David Grünwald, Sjoerd Stallinga, and Bernd Rieger. Measuring image resolution in optical nanoscopy. 10(6):557–562. ISSN 1548-7091, 1548-7105. doi: 10.1038/nmeth.2448.
37. Martin Ovesný, Pavel Křížek, Josef Borkovec, Zdeněk Švindrych, and Guy M. Hagen. ThunderSTORM: a comprehensive ImageJ plug-in for PALM and STORM data analysis and super-resolution imaging. 30(16):2389–2390. ISSN 1367-4803, 1460-2059. doi: 10.1093/bioinformatics/btu202.
38. Benjamien Moeyaert and Peter Dedecker. A comprehensive dataset of image sequences covering 20 fluorescent protein labels and 12 imaging conditions for use in super-resolution imaging. 29:105273. ISSN 23523409. doi: 10.1016/j.dib.2020.105273.
39. Benjamien Moeyaert, Wim Vandenberg, and Peter Dedecker. SOFIevaluator: a strategy for the quantitative quality assessment of SOFI data. 11(2):636. ISSN 2156-7085, 2156-7085. doi: 10.1364/BOE.382278.
40. Z. Wang, A.C. Bovik, H.R. Sheikh, and E.P. Simoncelli. Image quality assessment: From error visibility to structural similarity. 13(4):600–612. ISSN 1057-7149. doi: 10.1109/TIP.2003.819861.
41. Jonathan Nixon-Abell, Christopher J. Obara, Aubrey V. Weigel, Dong Li, Wesley R. Legant, C. Shan Xu, H. Amalia Pasolli, Kirsten Harvey, Harald F. Hess, Eric Betzig, Craig Blackstone, and Jennifer Lippincott-Schwartz. Increased spatiotemporal resolution reveals highly dynamic dense tubular matrices in the peripheral ER. 354(6311):aaf3928–aaf3928. ISSN 0036-8075, 1095-9203. doi: 10.1126/science.aaf3928.
42. Ralph Gräf, Jens Rietdorf, and Timo Zimmermann. Live cell spinning disk microscopy. In Jens Rietdorf, editor, *Microscopy Techniques*, volume 95, pages 57–75. Springer Berlin Heidelberg. ISBN 978-3-540-23698-6 978-3-540-31545-2. doi: 10.1007/b102210. Series Title: Advances in Biochemical Engineering/Biotechnology.
43. Bi-Chang Chen, Wesley R. Legant, Kai Wang, Lin Shao, Daniel E. Milkie, Michael W. Davidson, Chris Janetopoulos, Xufeng S. Wu, John A. Hammer, Zhe Liu, Brian P. English, Yuko Mimori-Kiyosue, Daniel P. Romero, Alex T. Ritter, Jennifer Lippincott-Schwartz, Lillian Fritz-Laylin, R. Dyche Mullins, Diana M. Mitchell, Joshua N. Bembenek, Anne-Cecile Reymann, Ralph Böhme, Stephan W. Grill, Jennifer T. Wang, Geraldine Seydoux, U. Serdar Tulu, Daniel P. Kiehart, and Eric Betzig. Lattice light-sheet microscopy: Imaging molecules to embryos at high spatiotemporal resolution. 346(6208):1257998. ISSN 0036-8075, 1095-9203. doi: 10.1126/science.1257998.
44. Stefan Geissbuehler, Azat Sharipov, Aurélien Godinat, Noelia L. Bocchio, Patrick A. Sandoz, Anja Huss, Nickels A. Jensen, Stefan Jakobs, Jörg Enderlein, F. Gisou van der Goot, Elena A. Dubikovskaya, Theo Lasser, and Marcel Leutenegger. Live-cell multiplane three-dimensional super-resolution optical fluctuation imaging. 5(1):5830. ISSN 2041-1723. doi: 10.1038/ncomms6830.
45. Thomas Mangeat, Simon Labouesse, Marc Allain, Awoke Negash, Emmanuel Martin, Aude Guénolé, Renaud Poincloux, Claire Estibal, Anaïs Bouissou, Sylvain Cantaloube, Elodie Vega, Tong Li, Christian Rouvière, Sophie Allart, Debora Keller, Valentin Debarnot, Xia Bo Wang, Grégoire Michaux, Mathieu Pinot, Roland Le Borgne, Sylvie Tournier, Magali Suzanne, Jérome Idier, and Anne Sentenac. Super-resolved live-cell imaging using random illumination microscopy. 1(1):100009. ISSN 26672375. doi: 10.1016/j.crmeth.2021.100009.

Supplementary Note 1: eSRRF parameters

Only four parameters need to be set upon reconstruction: a magnification M defines how the camera pixels are split into sub-pixels for the RGC estimation; a radius R defining the receptive field size that is used to calculate the RGC; a sensitivity value S that enables fine-tuning of the PSF sharpening power applied by the RGC, which is especially useful in low emitter density regimes; and a last parameter that defines the type of temporal analysis applied to the RGC image time series. Different parameter settings will yield best results in different regimes.

Supplementary Note 2: (e)SRRF and its artifacts

The presence of artifacts in the SRRF reconstruction have been observed previously(1). Here, we highlight an instance where they appear quite clearly. We generated a simulated dataset where the underlying fluorophore arrangement follows a fan configuration. Supplementary Fig. 2 shows the reconstructions obtained from SRRF and eSRRF, as well as quantitative measures of image quality based on our SQUIRREL method(2). We observe a clear visual and quantitative improvement of the method. Both RSP and RSE show values associated with improved quality.

Supplementary Note 3: eSRRF temporal analysis types

AVG: temporal average - Typically, it works best for sparse emitter datasets where the sharpening of PSFs via the radial symmetry transform is sufficient to produce higher resolution dataset VAR: temporal variance - Corresponds to cross-cumulant of 1st order without temporal offset TAC2: 2nd order temporal auto-cumulant corresponding to cross-cumulant of 1st order with offset of one frame(3).

Supplementary Tables

Method	Reference	Basic principles	Implementation	GPU acceleration	Image fidelity validated	3D	In depth
eSRRF	this publication	Radiality and temporal cross-correlation	Fiji	Yes	Yes	Yes	Yes
SRRF	Gustafsson *et al.*, 2016(4)	Radiality and temporal cross-correlation	Fiji	Yes	No	No	Yes
MUSICAL	Agarwal *et al.*, 2016(5)	Multiple signal classification	Fiji	Yes	No	No	Yes
SOFI	Dertinger *et al.*, 2009(6)	Temporal cross-correlation	MATLAB	No	No	Yes	Yes
SACD	Zhao *et al.*, 2020(7)	Deconvolution, temporal cross-correlation	MATLAB	No	No	No	?

Supplementary Table 1: Comparison of fluctuation-based super-resolution microscopy methods.

Supplementary Figures

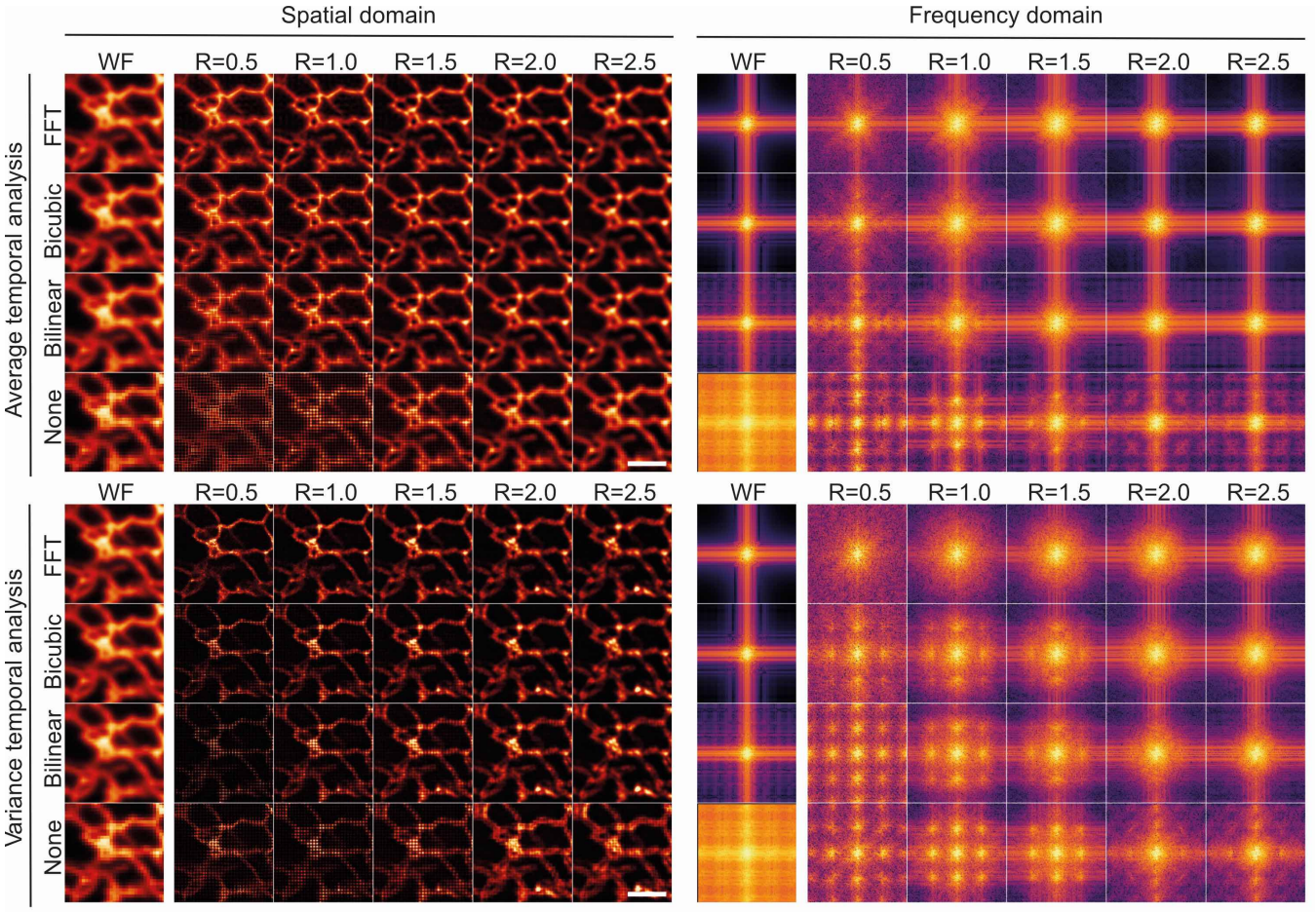

Fig. S1. Comparison of interpolation methods in the reconstruction of SRRF images. The presence of macro-pixel artifacts is apparent in both the spatial (left column), and frequency domain (right column) and for AVG (upper row) and VAR temporal analysis reconstruction (lower row) for all interpolation methods apart from the FFT-based interpolation. Data shown corresponds to live COS-7 cells expressing PrSS-mEmerald-KDEL acquired using HiLO-TIRF. Scale bars 2 µm.

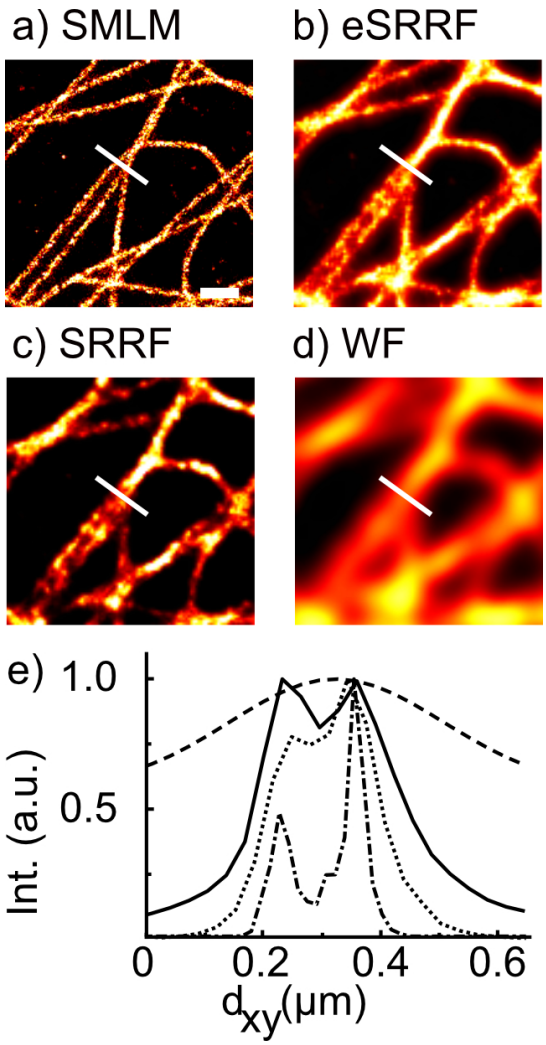

Fig. S2. Resolution improvement of eSRRF vs. SRRF. Image sections of the data set presented in Figure 1 after a) SMLM image reconstruction, b) eSRRF processing, c) SRRF processing and as WF data. The white line indicates the position of the line profiles. e) Intensity profiles allow to distinguish two filaments in the SMLM reconstruction (dash-dotted line) which can also be resolved with eSRRF (solid line) but the presence of a second filament is unclear in the case of SRRF processing (dotted line) and for the WF data (dashed line). Scale bar: 500 nm.

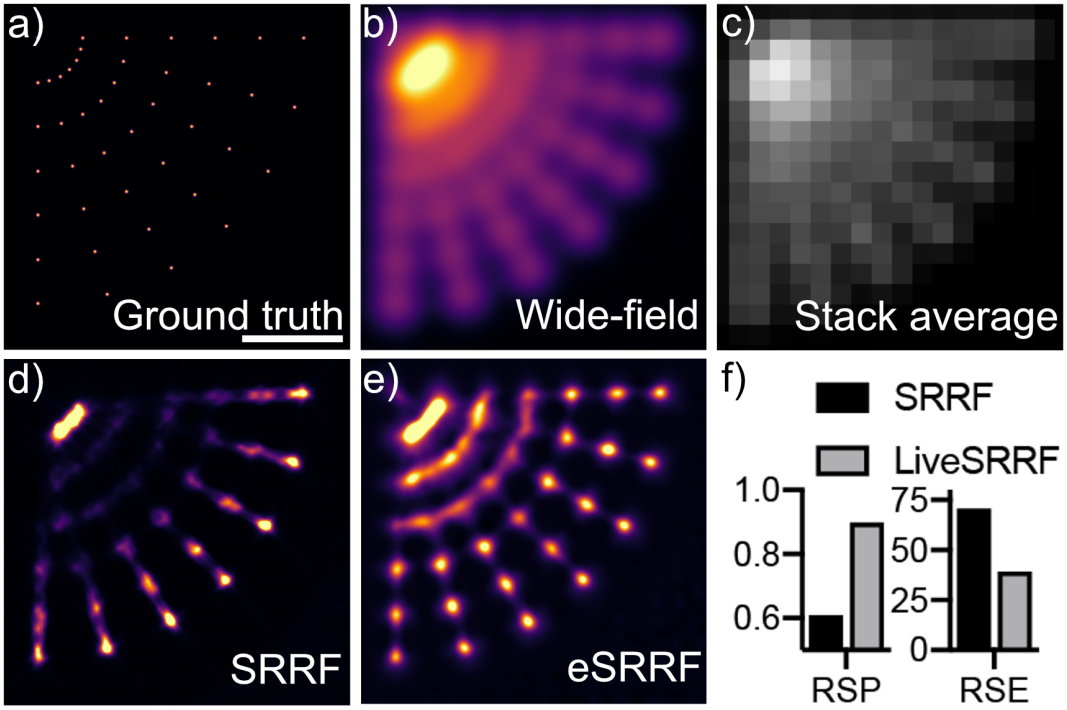

Fig. S3. Performance improvement of eSRRF on simulated data. a) Simulated ground truth indicating the positions of individual molecules in the image. b) Interpolated wide-field image. c) Average of all simulated raw frames. d) SRRF image. e) eSRRF image. f) Quantitative comparisons of SRRF and eSRRF based on RSP and Resolution Scaled Error (RSE) obtained from SQUIRREL. Artifacts like the linearity loss and and over sharpening as they are observed in d) are significantly reduced with e) eSRRF processing, Scale bar: 500 nm.

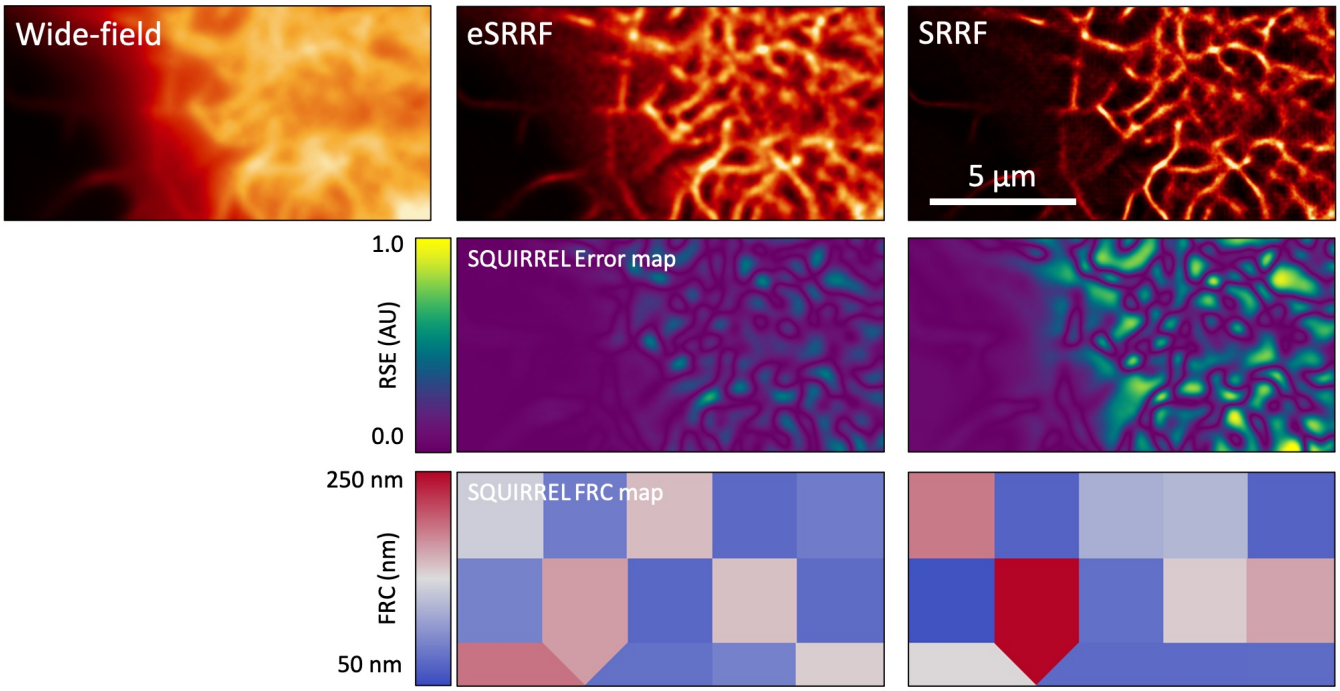

Fig. S4. SQUIRREL comparison of SRRF and eSRRF. eSRRF of the actin network (GFP-UtrCH expression, 100 frames at 33 frames/s) in live COS-7 cells shows an improved fidelity with a retained FRC resolution range. The dataset was published before in Culley et al.(8)

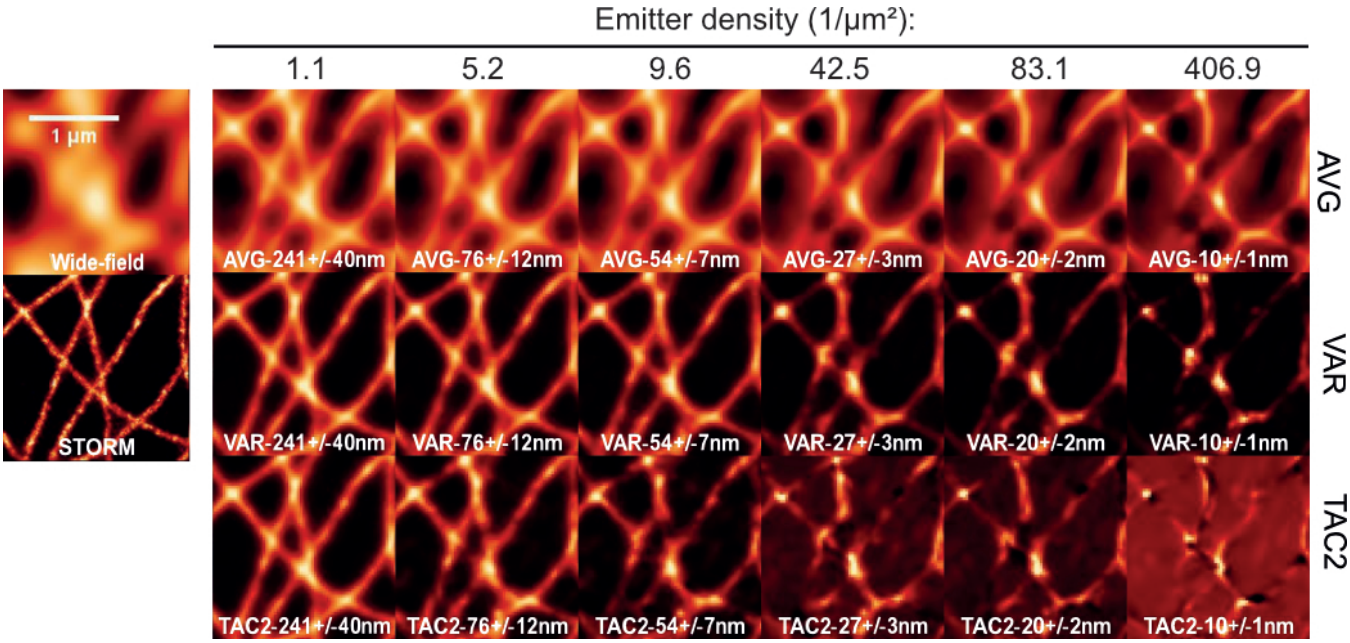

Fig. S5. Temporal analyses of eSRRF as a function of the density of emitters in the raw data images. The reconstructed images are shown in increasing emitter density from left to right. The corresponding average nearest-neighbor distance is stated in each panel. The wide-field and STORM equivalents are shown on the left for comparison. Scale bar 1 μm.

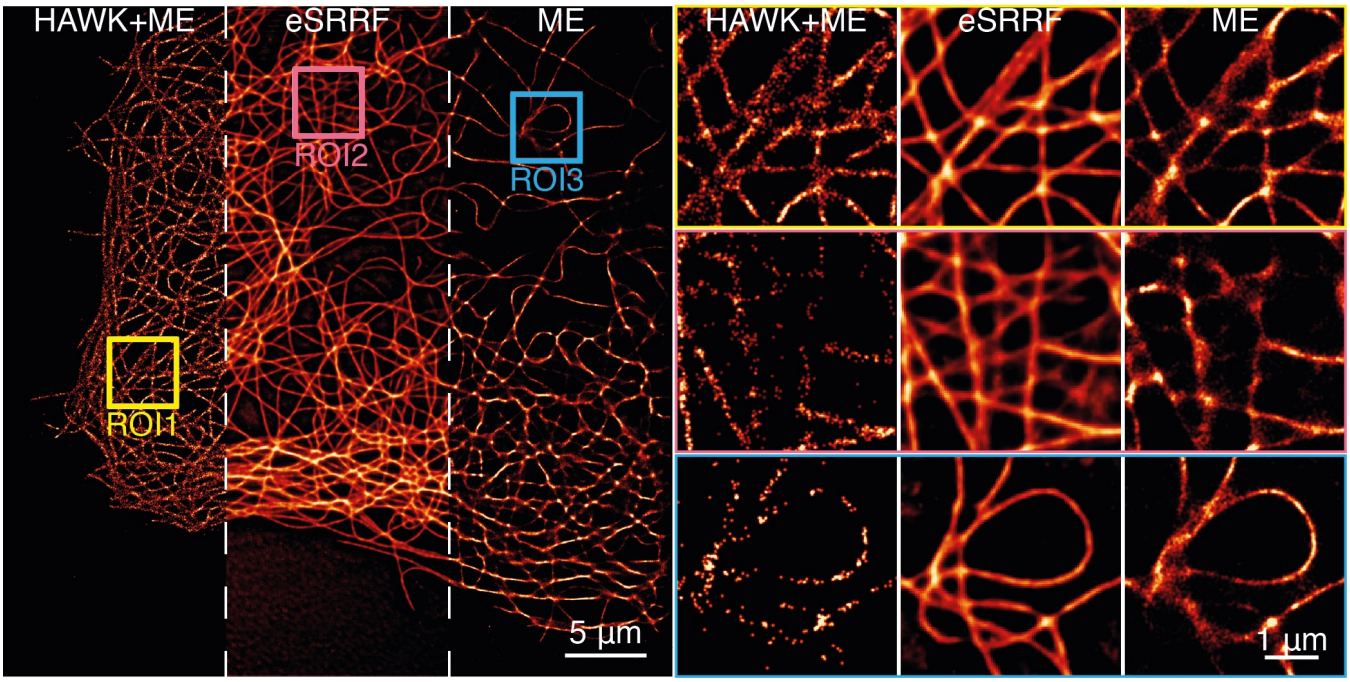

Fig. S6. Comparison of eSRRF, HAWK+ME and ME. The Maximum Likelihood Estimation multi-emitter fitting (ME) was performed using ThunderSTORM(9). Data shown corresponds to a DNA-PAINT acquisition of immunolabeled microtubules in fixed COS7 cells under TIRF illumination.

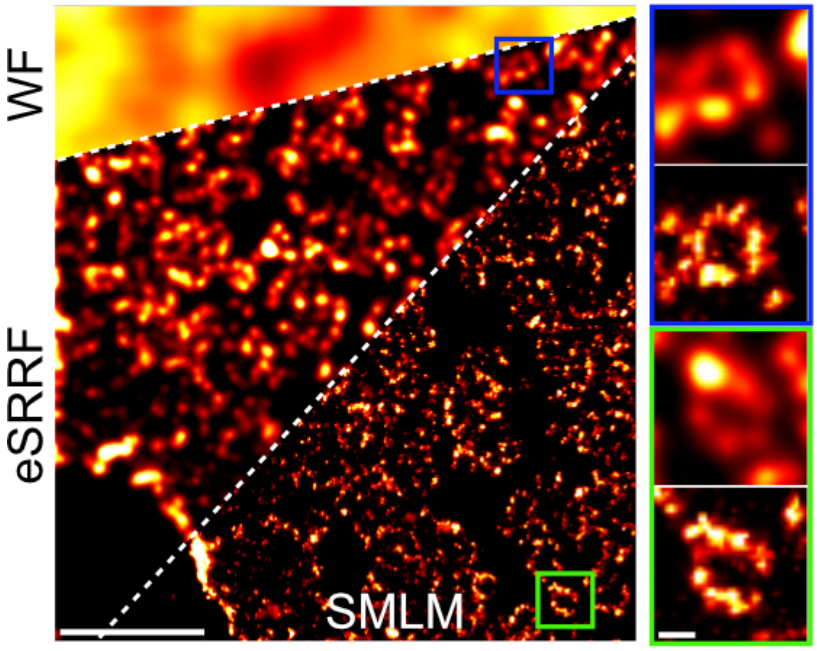

Fig. S7. eSRRF allows a fast preview of SMLM dataset reconstruction. Widefield imaging (top left) of the nuclear pore complex. Fast eSRRF reconstruction preview (first 2000 frames shown) reveals the open ring structure (left panel middle area and insets top panels). While fast eSRRF can resolve the central pore which has a diameter of about 140 nm, the full 8-element ring with only 40 nm gaps is only resolved by single-molecule localization analysis of the full 20 000 frames image stack (left panel bottom area and insets lower panels. The FRC resolution is 44.4±2.5 nm, and 35.1±6.3 for eSRRF and SMLM, respectively.,) (Dataset from Heil et al. (10)), left panel: scale bar 1 µm, insets on the right: scale bar 100 nm.

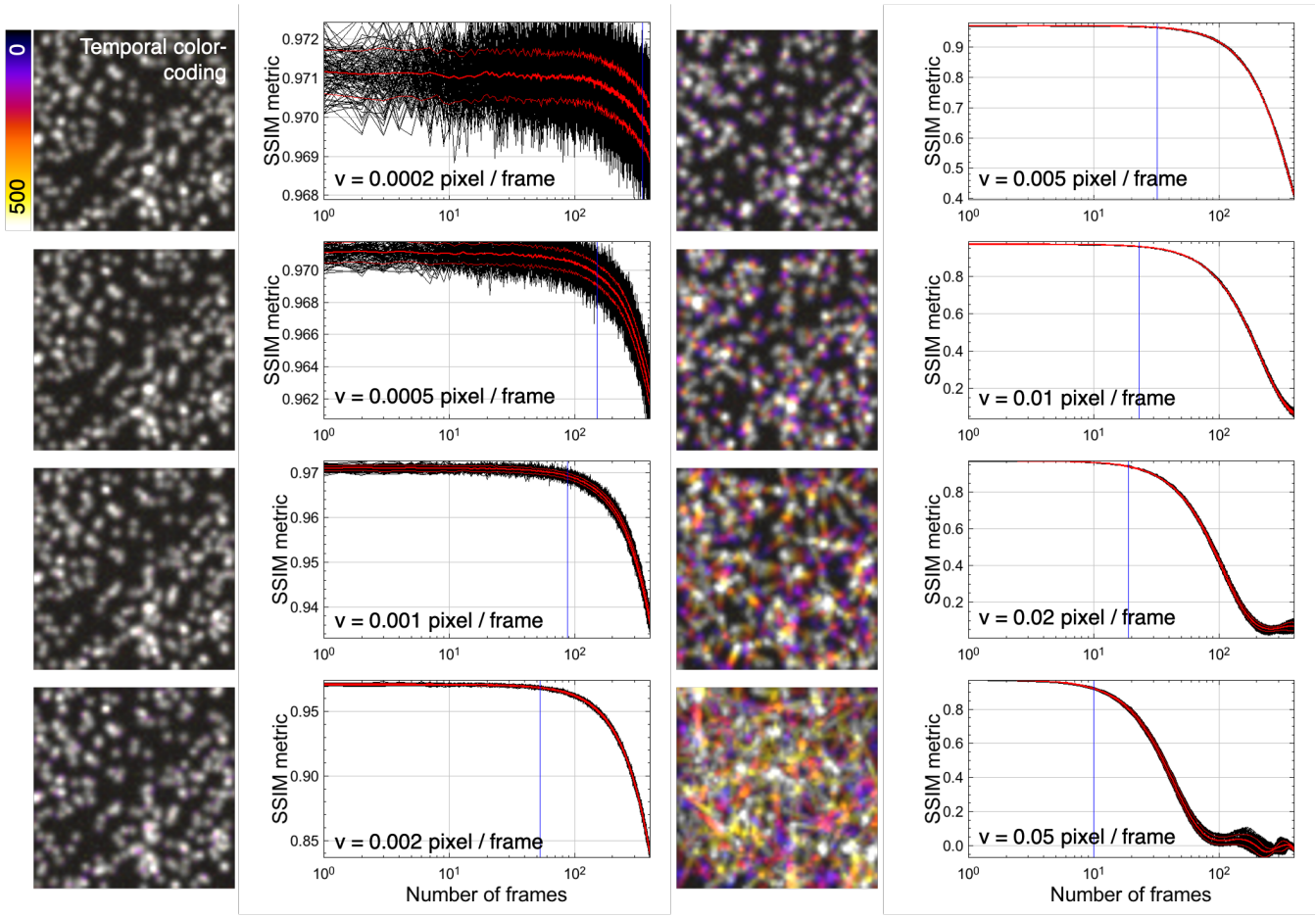

Fig. S8. tSSIM analysis of simulated moving particles. Color coded projections of simulated image stacks displaying particles diffusing with various speeds v and the resulting SSIM metric progression over time. The tSSIM metric shows sensitivity as a function of particle displacement per frame. This can be used to estimate the size of the optimal time window for eSRRF processing to avoid movement artifacts.

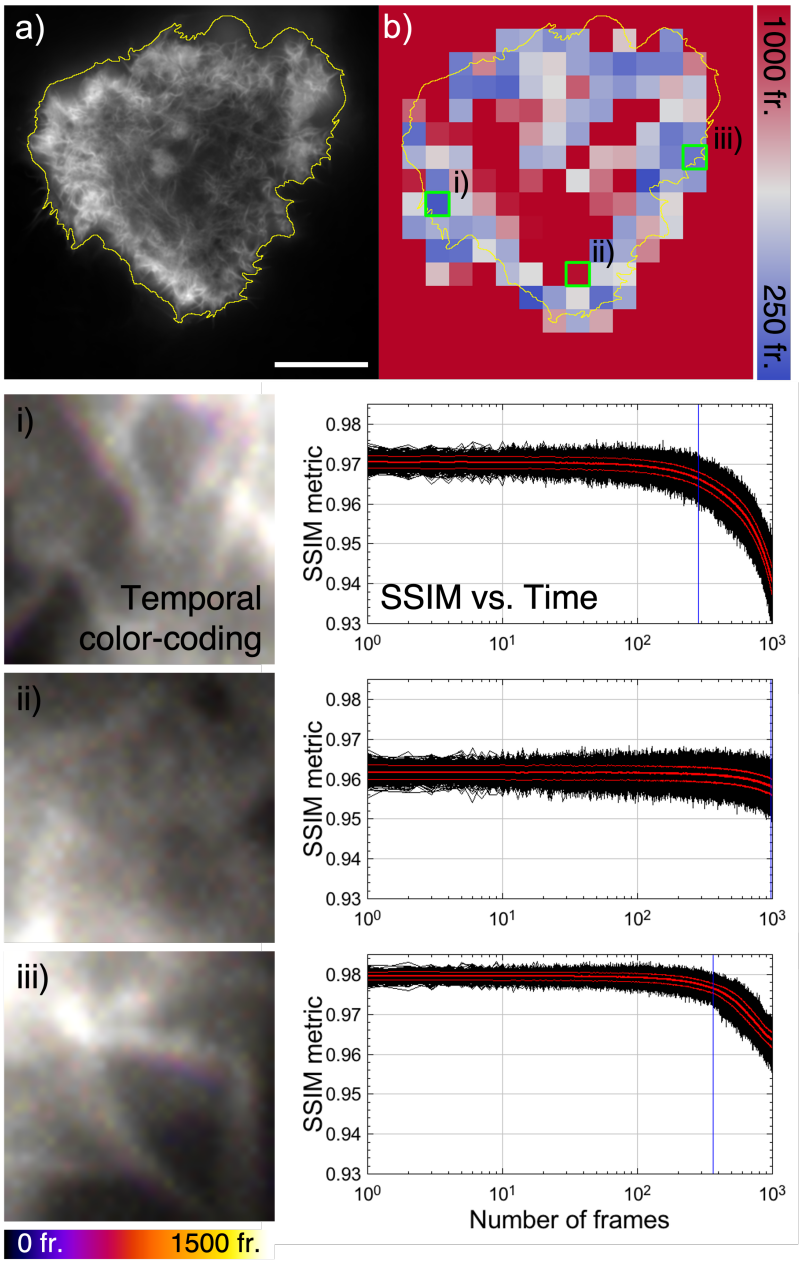

Fig. S9. tSSIM analysis performed over small image patches detects local dynamics of actin rearrangement in COS-7 cells. a) The actin network in live COS-7 cells expressing the marker GFP-UtrCH was acquired at 33 fps. b) The tSSIM metric estimates the time range of motion within individual subsections of a). The different subsections highlighted in green display the color-coded projection of regions with i) fast, ii) slow, and iii) moderate speeds as is also reflected by the corresponding progression of the SSIM metric over time. Scale bar 20 µm.

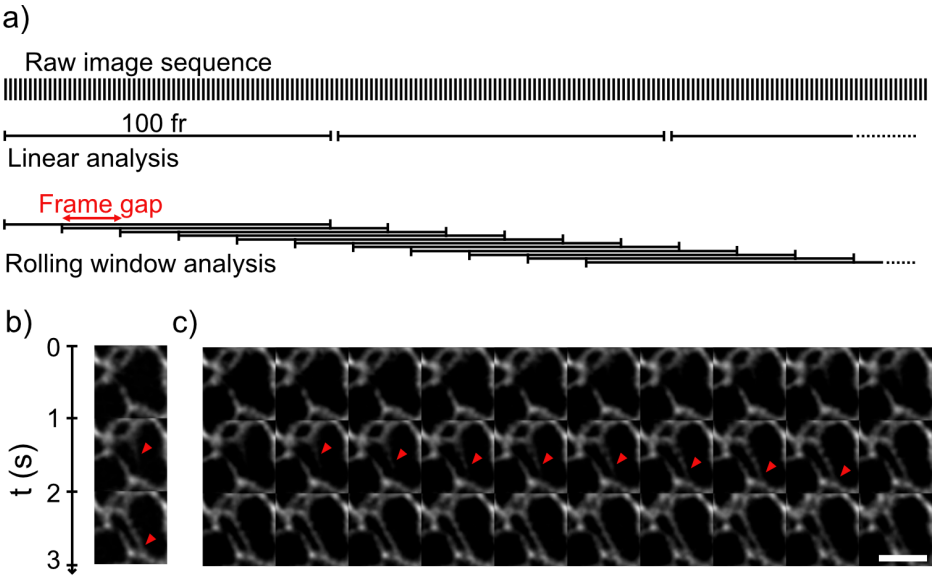

Fig. S10. Increasing temporal sampling by rolling window analysis. a) Super-resolved temporal image stack is reconstructed by analyzing consecutive frame windows (linear analysis). A rolling window analysis with a frame gap of less than the window size allows to increase the temporal sampling rate and can translate into a higher temporal resolution without sacrificing spatial resolution. b) This allows to visualize dynamic rearrangement of the endoplasmic reticulum (ER, red arrow) acquired by live-cell HiLO-TIRF of COS-7 cells expressing PrSS-mEmerald-KDEL at a frame rate of 1 Hz with a 100 fr-window linear eSRRF analysis. c) The rolling window analysis with a frame gap of 10 fr allows to increase the temporal sampling to 10 Hz, thus, revealing the substeps of the ER tubule formation (red arrow), image section width 3 µm, FRC resolution: eSRRF: 143±56 nm, Scale bar 2 µm.

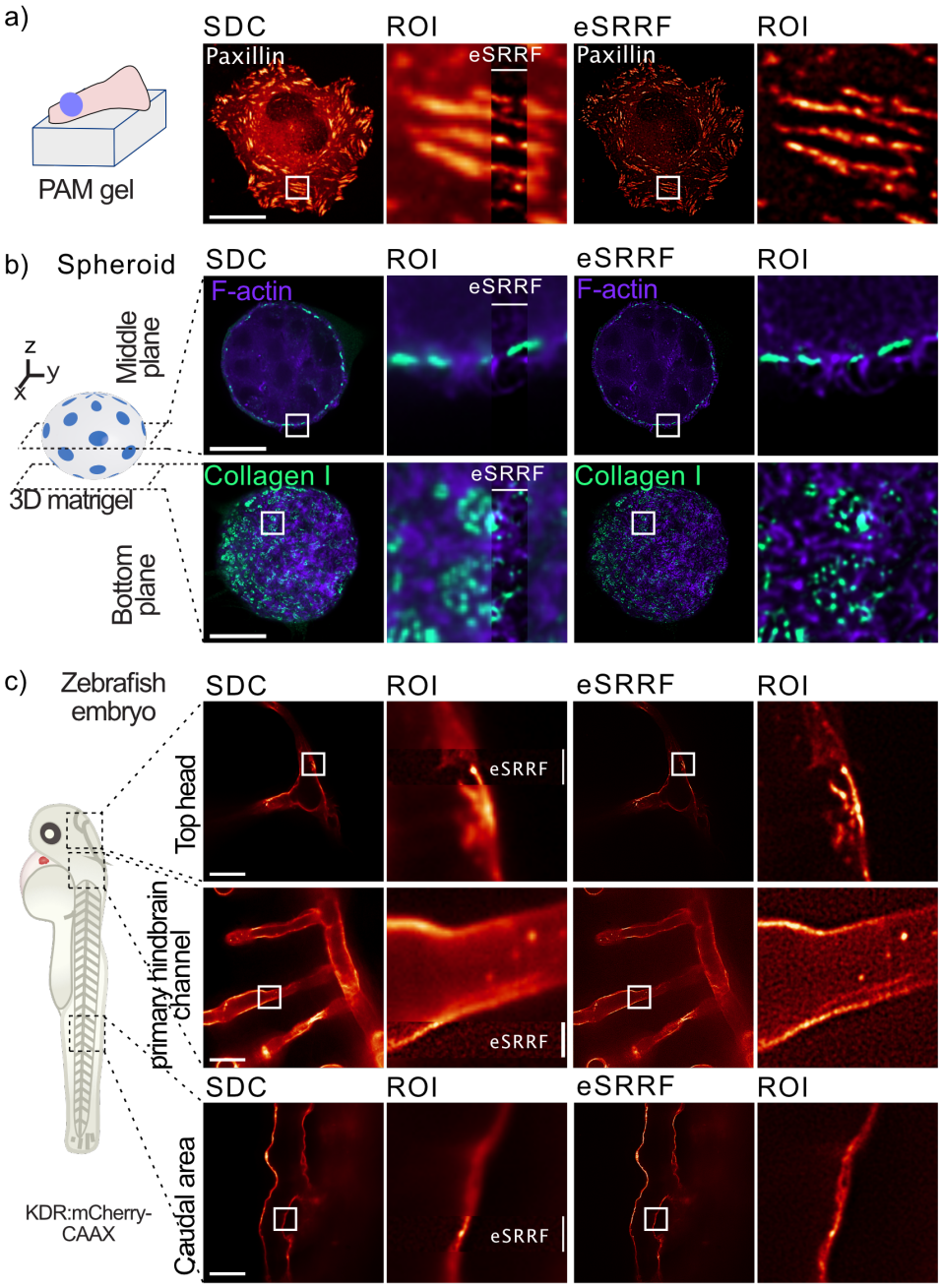

Fig. S11. eSRRF enhances spinning-disk confocal imaging deep inside fixed and live cells, spheroid and organisms. a) U2OS cells expressing endogenously tagged paxillin were plated on 9.6 kPa polyacrylamide (PAM) gels and were imaged live using a spinning-disk confocal (SDC). b) DCIS.com lifeact-RFP cells forming a spheroid in 3D matrigel in the presence of fluorescently labeled collagen I. Samples were fixed and imaged using a spinning-disk confocal microscope and processed using eSRRF. Representative fields of view highlighting the spheroids' middle and bottom planes are displayed. c) Zebrafish embryos expressing mcherryCAAX in the endothelium were imaged live using a spinning-disk confocal. Vessels located at different parts of the embryo were imaged. For all panels, the eSRRF reconstructed images and the original spinning disk images are displayed. Scale bars 25 µm.

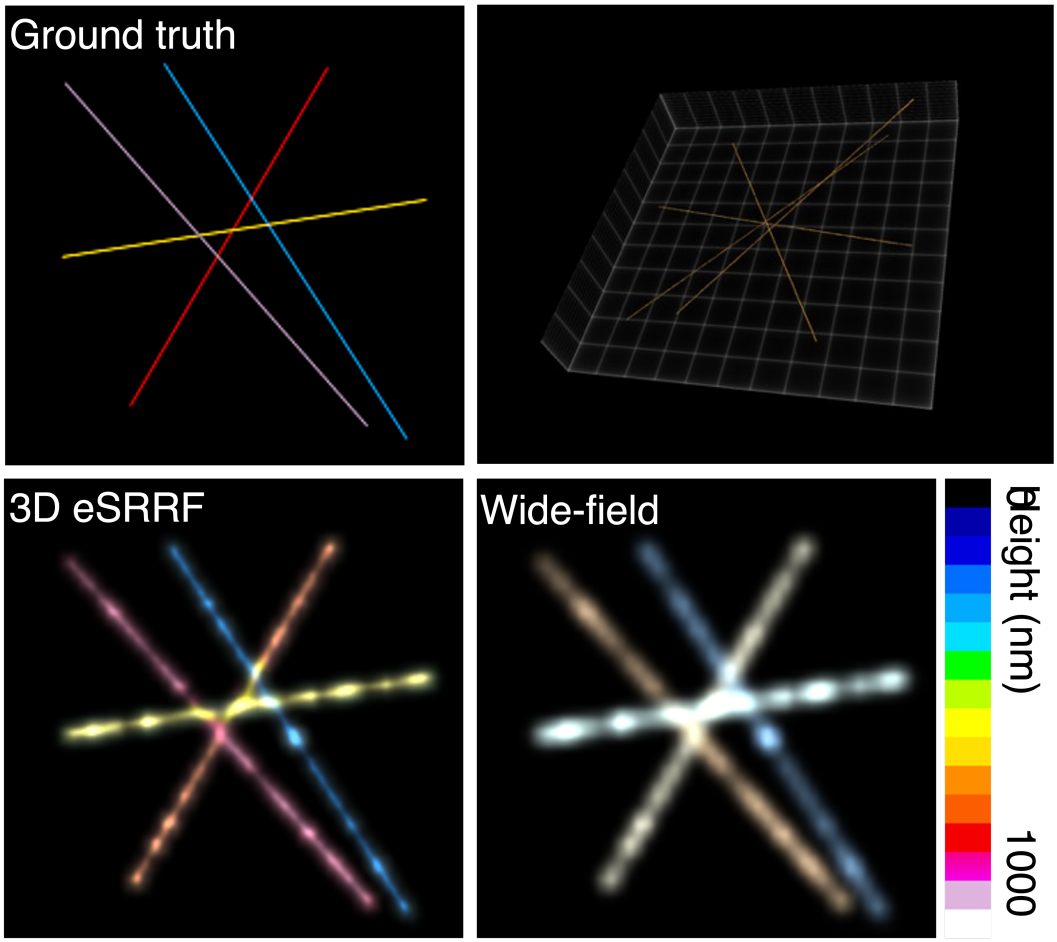

Fig. S12. 3D eSRRF on a simulated dataset. The height of the filament is color coded as indicated by the false color scale.

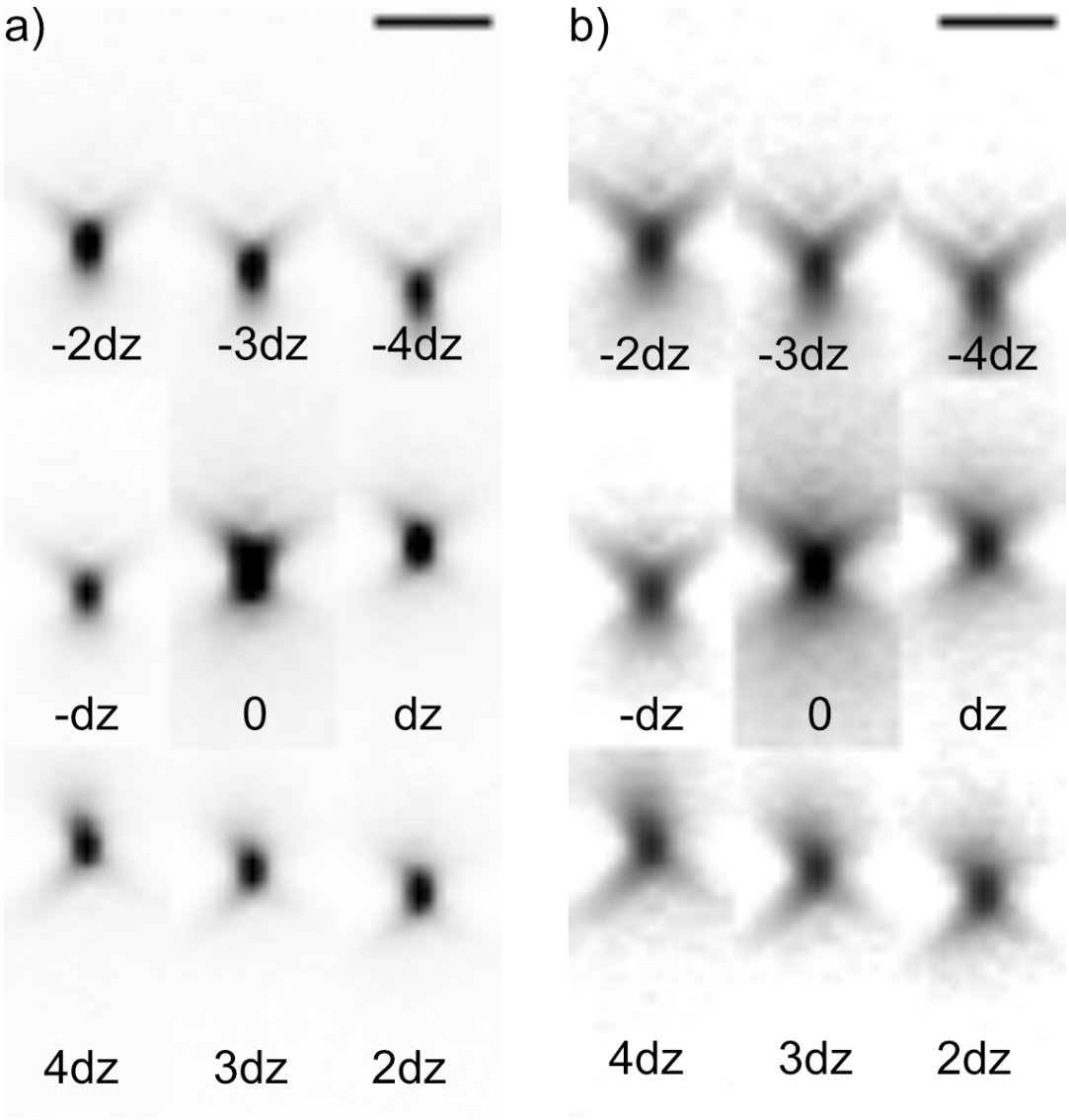

Fig. S13. 3D PSF in the nine focus planes of the MFM displays only minor aberrations and good radial symmetry. x-z view of the PSF mapped with the bead calibration dataset displayed in a) linear and b) logarithmic brightness scale (FWHMX=431±19 nm, FWHMz=704±45 nm). The focus offset dz between each focal plane is 390 nm. Scale bars 2 µm.

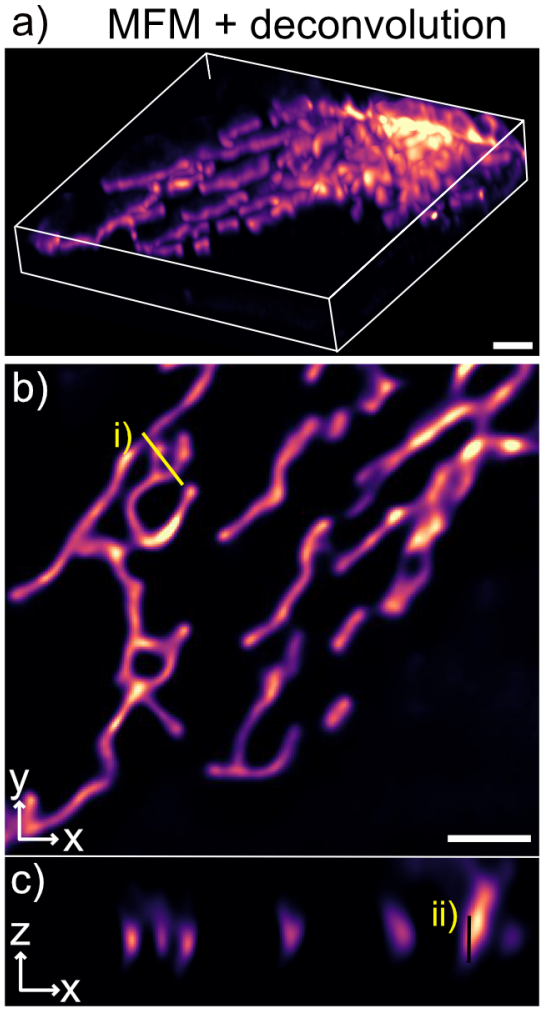

Fig. S14. Deconvolved 3D image stack of U2OS cells expressing TOM20-Halo, loaded with JF549 acquired with MFM. a) 3D rendering, b) single z-slice and c) single cropped y-slice. i) and ii) are the line profiles in x,y and z-plane displayed in Figure 4. Scale bars 2 µm.

Supplementary Movies

Supplementary Movie S1.: Lattice-light sheet imaging of ER in live Jurkat cells enhanced by eSRRF. .

Supplementary Movie S2.: Live-cell 3D eSRRF of mitochondria dynamics with MFM. Live-cell volumetric imaging of U2OS cells expressing TOM20-Halo, loaded with JF549 with MFM of a 20 x 20 x 3.6 µm3 at a volume frequency of 1Hz, the grid size is 2 µm.

Supplementary Movie S3.: Observing mitochondria dynamics with live-cell 3D eSRRF with MFM. Single z slice image over the whole MFM acquisition time of U2OS cells expressing TOM20-Halo loaded with JF549, before (left) and after eSRRF processing (right). Scale bar 2 µm..

Supplementary Bibliography

1. Richard J. Marsh, Karin Pfisterer, Pauline Bennett, Liisa M. Hirvonen, Mathias Gautel, Gareth E. Jones, and Susan Cox. Artifact-free high-density localization microscopy analysis. 15(9):689–692. ISSN 1548-7091, 1548-7105. doi: 10.1038/s41592-018-0072-5.
2. Siân Culley, David Albrecht, Caron Jacobs, Pedro Matos Pereira, Christophe Leterrier, Jason Mercer, and Ricardo Henriques. Quantitative mapping and minimization of super-resolution optical imaging artifacts. 15(4):263–266, . ISSN 1548-7091, 1548-7105. doi: 10.1038/nmeth.4605.
3. J.M. Mendel. Tutorial on higher-order statistics (spectra) in signal processing and system theory: theoretical results and some applications. 79(3):278–305. ISSN 00189219. doi: 10.1109/5.75086.
4. Nils Gustafsson, Siân Culley, George Ashdown, Dylan M. Owen, Pedro Matos Pereira, and Ricardo Henriques. Fast live-cell conventional fluorophore nanoscopy with ImageJ through super-resolution radial fluctuations. 7(1):12471. ISSN 2041-1723. doi: 10.1038/ncomms12471.
5. Krishna Agarwal and Radek Macháň. Multiple signal classification algorithm for super-resolution fluorescence microscopy. 7(1):13752. ISSN 2041-1723. doi: 10.1038/ncomms13752.
6. T. Dertinger, R. Colyer, G. Iyer, S. Weiss, and J. Enderlein. Fast, background-free, 3d super-resolution optical fluctuation imaging (SOFI). 106(52):22287–22292. ISSN 0027-8424, 1091-6490. doi: 10.1073/pnas.0907866106.
7. Weisong Zhao, Jian Liu, and Haoyu Li. Ultrafast super-resolution imaging via auto-correlation two-step deconvolution. In *Ultrafast Nonlinear Imaging and Spectroscopy VIII*, volume 11497, pages 42–49. SPIE. doi: 10.1117/12.2567853.
8. Siân Culley, Kalina L. Tosheva, Pedro Matos Pereira, and Ricardo Henriques. SRRF: Universal live-cell super-resolution microscopy. 101:74–79, . ISSN 13572725. doi: 10.1016/j.biocel.2018.05.014.
9. Martin Ovesný, Pavel Křížek, Josef Borkovec, Zdeněk Švindrych, and Guy M. Hagen. ThunderSTORM: a comprehensive ImageJ plug-in for PALM and STORM data analysis and super-resolution imaging. 30(16):2389–2390. ISSN 1367-4803, 1460-2059. doi: 10.1093/bioinformatics/btu202.
10. Hannah S. Heil, Benjamin Schreiber, Ralph Götz, Monika Emmerling, Marie-Christine Dabauvalle, Georg Krohne, Sven Höfling, Martin Kamp, Markus Sauer, and Katrin G. Heinze. Sharpening emitter localization in front of a tuned mirror. 7(1):99. ISSN 2047-7538. doi: 10.1038/s41377-018-0104-z.